

# Enhancing the Prediction of Locomotion Transition with High-Density Surface Electromyography

Shibo Jing, Hsien-Yung Huang, *Member, IEEE*, Melanie Jouaiti, Yongkun Zhao, Zhenhua Yu, Ravi Vaidyanathan, *Member, IEEE*, and Dario Farina, *Fellow, IEEE*

**Abstract**—Prediction of transition between locomotion modes (e.g. moving from flat ground to stairs, etc) is vital for optimal interface with lower limb assistive technologies such as exoskeletons and prostheses. Inertial and bipolar electromyography (EMG) sensors have been investigated, but accuracy for clinical utility remains unresolved. This shortfall may be attributed to their limited capacity to detect subtle changes in muscle activations, particularly during the early stages of locomotion transitions (e.g., near the toe-off). In this study, we examined the effectiveness of two high-density surface electromyography (HDsEMG) sensors in detecting muscle activation changes during stair-related transitions. The results revealed that compared to bipolar EMG on the same muscles, HDsEMG-based methods increased transition prediction accuracy significantly from 70.2% to 91.1% when predicting at toe-off and from 89.8% to 99.2% when predicting with a delay of 400-ms relative to toe-off. This demonstrated the superior ability of HDsEMG to capture subtle muscle activation changes, especially during early transition stages. We also found reducing the electrode count to 21 per muscle only minimally impacted performance (88.3% accuracy at toe-off). This suggests distributing the same total number of electrodes across more muscles could potentially further improve prediction accuracy without increasing computational load. Moreover, by implementing image-inpainting signal processing, HDsEMG demonstrated robustness against the common issue of electrode signal loss. Even with 30% electrode detachment, prediction accuracy decreased only by 3%. We argue that HDsEMG offers a promising solution to bridge the gap in locomotion transition prediction for interface with assistive technology.

This research was supported by EPSRC grant: EP/T020970/1, NIS-NEM, and the UK Dementia Research Institute (UK DRI-7003, UK DRI-7005) principally funded by the Medical Research Council, in partnership with Alzheimer's Society. Corresponding author: Dario Farina.

S.Jing and R.Vaidyanathan are with the Department of Mechanical Engineering and the Dementia Research Institute Care Research & Technology Centre (DRI-CR&T), Imperial College London, London, United Kingdom (e-mail: s.jing19@imperial.ac.uk, z.yu18@imperial.ac.uk, r.vaidyanathan@imperial.ac.uk).

H.Y.Huang is with the Department of Engineering and Design, University of Sussex, Sussex, United Kingdom (e-mail: HsienYung.Huang@sussex.ac.uk).

M.Jouaiti is with the School of Computer Science, University of Birmingham, Birmingham, United Kingdom (e-mail: m.jouaiti@bham.ac.uk).

Z.Yu is with the Department of Computer Science, University of Aberdeen, Aberdeen, United Kingdom (e-mail: zhenhua.yu@abdn.ac.uk).

Y.Zhao and D.Farina are with the Department of Bioengineering, Imperial College London, London, United Kingdom (e-mail: y.zhao22@imperial.ac.uk, d.farina@imperial.ac.uk ).

**Index Terms**—high-density sEMG; locomotion transition prediction; CNN; GRU; electrode loss

## I. INTRODUCTION

TECHNOLOGICAL advancements have fostered increasing interests in human-machine interaction for applications such as exoskeletons and prostheses to aid human movement. A critical component of these applications to the lower limb is to accurately identify human locomotion states, to facilitate prompt and safe walking assistance through appropriate robotic control.

Locomotion states can be broadly classified into steady states and transitional states [1]. Steady states represent the period of continuous walking in a consistent locomotion mode, such as a series of gait cycles during the level walking mode or the stair ascent mode. Transitional states represent the period of shifting between different locomotion modes, such as from the level walking mode to the stair ascent mode. In general, identifying current locomotion modes during steady states is a recognition problem (locomotion recognition), whereas predicting the next locomotion mode during transitional states is a prediction problem (transition prediction).

While many studies have achieved significant progress using mechanical sensors and bipolar EMG in both upper limb [2] and lower limb motion recognition [3]–[5], predicting transitions between locomotion modes remains challenging. As transitional states are short, it is crucial to accurately predict within this short period, preferably as early as possible. Delayed identification may lead to late mode switching in devices such as exoskeletons or prostheses, resulting in serious consequences for the user, including a pronounced sluggish feeling and an increased risk of falls.

Various methods have been developed to address the transition prediction problem in human movement. Su et al. [6] utilized a CNN model with data from three IMUs on the thigh, shank, and foot to classify 13 locomotion classes, including five steady states and eight transitional states, and achieved 94.5% accuracy with around 500 ms delay after toe-off. In addition to mechanical sensors, bipolar EMG has also been explored for transition prediction. Recently, Camargo et al. [7] integrated data from IMUs, goniometers (GONs), and bipolar EMG sensors to classify ambulation modes (level-

ground, ramps, and stairs), achieving 99% accuracy for steady-state modes and 96% for transitions (the delay has not been reported). Liu et al. [8] combined bipolar EMG and IMU data to classify five walking modes, considering variations in walking speed and ramp inclination. They employed a muscle synergy-inspired method for classification and obtained an overall accuracy of 94.5%, with the predictions made around 300ms prior to the next step's heel strike.

It is noteworthy that the aforementioned research has already employed numerous wearable sensors covering the entire lower limb muscle, such as 11 bipolar EMG sensors, 3 GONs and 4 IMUs, unilaterally mounted [7], 20 bipolar EMG sensors and 7 IMUs, bilaterally mounted [8], and 14 bipolar EMG, 4 GONs and 4 IMUs, bilaterally mounted [9]. The sensor placement in their experimental setups is nearing saturation, which limits the possibility of integrating additional sensors. However, even the use of such numerous sensors has not yielded performance adequate for practical applications. For instance, a 95% accuracy implies an average of five incorrect modes switching out of every 100. Such inaccuracies, over long-term use, can lead to a significant number of erroneous mode switches in assistive devices, potentially harming the user. Furthermore, advancing the prediction time to earlier transition moments, e.g., ensuring accurate predictions near the toe-off, could provide more time for the robotic system to switch operation states during transitions, enhancing both smoothness and user safety. Thus, a further improvement in transition prediction is necessary, in both accuracy and response time.

To enhance prediction accuracy and response time, the sensor usage should be optimized. However, mechanical sensors, such as IMUS and GONs, respond after limb movement, typically functioning better in later transition stages when movement changes become evident. In comparison, bipolar EMG sensors acquire muscle activation signals that occur before body movement, which is expected to outperform mechanical sensors. However, previous research [7], [8], [10] indicated that bipolar EMG-based prediction did not surpass IMU-based approaches. This may be attributed to the early-stage EMG signal changes being too subtle for bipolar EMG to discern, hindering its ability to differentiate between locomotion modes. Thus, adopting a method that captures more detailed EMG signals could be a promising direction to pursue.

We propose HDsEMG as a potentially superior alternative to bipolar EMG to capture subtle changes from early transition stages. HDsEMG provides both spatial and temporal muscle activity information by employing multiple electrodes within a confined muscle area [11]. Given the larger skin surface coverage, HDsEMG may detect more detailed muscle activation, potentially identifying distinct patterns of various locomotion transitions that are undetectable with bipolar EMG.

HDsEMG has previously been utilized for upper limb motion recognition [12], [13]. The findings indicated that HDsEMG data contains discernible patterns that can differentiate gestures. Recently, Jing et al. [14] also employed HDsEMG for lower limb movement recognition, utilizing a single HDsEMG grid on the rectus femoris muscle to classify six steady-state locomotion modes, achieving an accuracy of around 97%.

However, no study has been found utilizing HDsEMG for locomotion transition prediction.

In this work, we utilized two HDsEMG sensors to examine their efficacy in identifying muscle activation changes during early transitions for predicting locomotion mode. Particularly, we were focusing on stair-related transitions, including the switch between level walking, stair ascent, stair descent, and standing still. Stair-associated transitions present a substantial risk of falls and necessitate early prediction; this is more crucial than other common daily scenarios, such as ramps, where a relatively late prediction poses a lower risk.

To our knowledge, this is the first study to investigate the use of HDsEMG for enhancing locomotion transition prediction. A cohesive set of results demonstrated the superiority of HDsEMG in accurately predicting the transitions. The main contributions of this work are: 1) Comparison of various classification models to evaluate the prediction performance of HDsEMG signals in locomotion transition. 2) Performance comparison between HDsEMG and bipolar EMG signals recorded from the same muscles to demonstrate the superior capability of HDsEMG. 3) Analysis of the impact of channel number, muscle number, and delay time on prediction performance, with recommendations for the optimal number of channels employed per muscle. 4) Introduction of an image-inpainting method to address the challenge of electrode signal loss in HDsEMG use in locomotion transition prediction, demonstrating the capacity to recover lost EMG channels based on the remaining channels of HDsEMG for enhanced robustness.

## II. EXPERIMENT

### A. Experiment Setup

Nine able-bodied subjects (six males and three females, aged 20-32 years, height ranging from 156 cm to 182 cm, and body mass between 43 kg and 78 kg) participated in the experiment. The experimental protocol was approved by the Imperial College Research Ethics Committee (ethical approval number: 18IC4685).

Two 64-monopolar electrode grids (GR08MM1305, OT Bioelettronica) with an 8-mm inter-electrode distance were used to record HDsEMG signals from the left leg muscles, specifically the rectus femoris (RF) and tibialis anterior (TA) muscles (Fig. 1a). These two muscles are large and easily accessible, yielding strong and consistent EMG signals, and have been frequently used in locomotion-related research. Prior to electrode placement, the skin area had been shaved and cleaned using abrasive paste and alcohol. Then conductive cream was applied to the grid for reliable contact between the skin and electrodes. The electrode placement followed the guideline of SENIAM [15].

EMG signals were sampled at 2000 Hz using two 64-channel HDsEMG devices (Sessantaquattro, OT Bioelettronica), and transmitted via Wi-Fi communication. A pair of pressure insoles (Stridalyzer PRISM, ReTiSense) were placed under the feet to measure the ground reaction force (GRF) for detecting gait events such as toe-off. The insole area was covered by a piezo-resistive force sensor array containing around

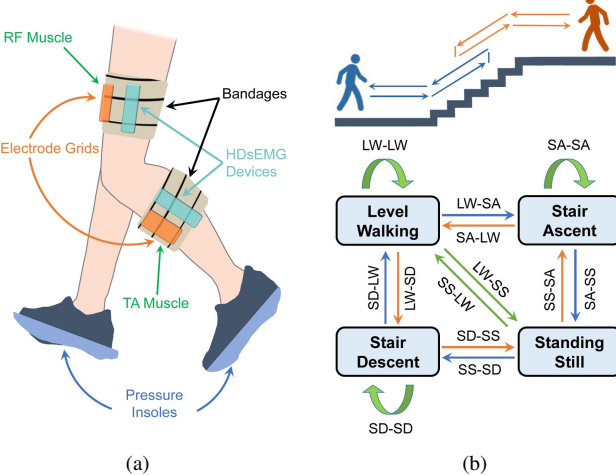


Fig. 1. Experiment description. In (a), the electrode grids were secured using surgical adhesive tapes and self-adhesive bandages, and the HDsEMG devices were fastened on the leg using self-adhesive bandages to reduce movement during walking. The device weighs only 110g and does not affect normal movement. (b) The transitions in experiments (e.g., LW-SA means transitioning from LW to SA). The experiments comprised two types of walking sequences: one involved the sequence of standing still (SS), level walking (LW), stair ascending (SA), standing, stair descending (SD), level walking, and standing again, as depicted in the blue trajectory on the top image; and the other was a reverse progression, as shown in the orange trajectory on the top image. The bottom image used three colors to mark transitions: blue arrows for transitions specific to the blue walking sequence, orange arrows for transitions specific to the orange walking sequence, and green arrows for transitions shared by both walking sequences.

60 sensors (each 12.5mm × 12.5mm), evenly distributed in each direction. The force signals were sampled at 50 Hz and transmitted via Bluetooth. All signals were synchronized and saved for offline analysis.

### B. Experiment Protocol

The experiment examined transitions between level walking, stair ascent, stair descent, and standing still, consisting of two parts. The first part is illustrated by the blue-colored trajectory in the top image of Fig. 1b. Participants began by standing still for 5 seconds and then initiated level walking with their left leg (instrumented leg). The level walking distance allowed two complete gait cycles before reaching a staircase. After reaching it, they transitioned to start ascending, using the left leg as the leading leg. Each step of the staircase is 17 cm high and 25 cm deep. Upon placing the right foot on the fourth step, participants then transitioned from stair ascent to standing with the left foot striding on the fourth step instead of continuing to walk. Then, they stood for 3 seconds, turned around, and stood for an additional 3 seconds.

Afterwards, participants were instructed to descend the staircase leading with the left leg again. Once the right foot touched the ground, the left leg then transitioned from stair descent to level walking. After two more gait cycles, they stopped walking, using the left leg to transition from level walking to standing. A completion of this sequence was called a session, and 30 sessions were recorded for each subject. A similar process was applied to the second part, in

which participants progressed from an opposite direction, first descending and then ascending. This is depicted by the orange-colored trajectory in the top image of Fig. 1b.

The experiment was designed to maintain the instrumented leg as the leading leg for all transitions. This enables the effective utilization of signals recorded from the instrumented leg for transition prediction. A metronome (set to 100 BPM) was held by an experimenter to maintain a consistent cadence. Breaks were allowed between sessions to avoid muscle fatigue. All transitions involved in the experiments are illustrated in the bottom image of Fig. 1b.

## III. METHODS

### A. Signal Preprocessing

A 4th order Butterworth bandpass filter with cut-off frequencies of 20 Hz - 400 Hz was utilized to filter each channel of the HDsEMG signals. The 64-channel electrode grid utilized has a  $13 \times 5$  shape with positions for 65 electrodes, but one corner electrode was missing due to the grid design. We replaced the missing electrode value by taking the average value of its surrounding electrodes. This resulted in a total of 65 channels, forming a  $13 \times 5$  array, which can be conveniently processed as a matrix or image.

Given that human locomotion frequency is typically below 4 Hz [16], a 4th order Butterworth lowpass filter with a cut-off frequency of 20 Hz was applied to the GRF signals. Subsequently, the GRF signals were upsampled to 2000 Hz for alignment with the HDsEMG signals. GRF signals supplied the toe-off timestamps, which were utilized to extract EMG data surrounding the toe-off moment for subsequent analysis. Finally, the extracted EMG data were downsampled to 1000 Hz to reduce memory consumption and speed up model training while maintaining performance. The GRF signals were solely used for gait event detection but were not provided as input into the model for classification.

### B. Analysis Windows

A time range of 850ms (450ms before and 400ms after the toe-off event) was used to extract event-specific EMG data for offline processing. Within the selected range, two types of windows were utilized: feature window and prediction window, as shown in Fig. 2.

1) *Feature Windows*: Feature windows were used for extracting EMG features from HDsEMG signals. Each window spans 350ms with a 20ms increment, which was found to be optimal in our testing scenario. Further increases in window length or decreases in increment offered only marginal benefits in our case but incurred higher computational costs. The sliding windows with overlapping were utilized as a data augmentation technique to increase the number of available training data for better classification results [17]. We adopted two distinct approaches to extract features from these windows: a manual feature engineering method and a CNN feature learning method.

For the conventional manual feature engineering method, eight time-domain features, commonly used in EMG-based classification applications [1], [18]–[20], were extracted from

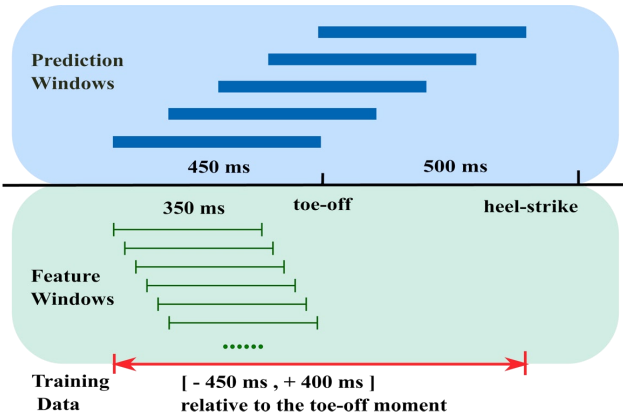


Fig. 2. Windows for feature extraction and prediction. Each prediction window contained six feature windows. Training data were extracted from 450 ms before and 400 ms after the toe-off moment.

each channel as model inputs: mean absolute value(MAV), root mean square(RMS), waveform length(WL), slope sign changes(SSC), zero-crossings(ZC), and third-order autoregressive coefficients(AR).

For the CNN feature learning method, manual pre-extraction of EMG features was not required. Instead, instantaneous HD-SEMG data were directly input into the classification model, and the CNN layers automatically extracted temporal-spatial features from the input data. More details will be presented in Section III-D.

**2) Prediction Windows:** Prediction windows were employed for decision making. Each prediction window spans 450ms, comprising six consecutive feature windows. We implemented two different approaches to make a final prediction decision based on these six feature windows: a many-to-one gated recurrent unit (GRU) method and a majority vote method.

The many-to-one GRU method treats six feature windows as a sequence of inputs, with each feature window representing one time step, and produces a single prediction output. GRU layers were expected to further capture additional temporal information from the consecutive feature windows to improve the prediction accuracy.

In contrast, when not using GRU layers, each of the six feature windows operates separately, leading to six independent prediction results. Then, a majority vote (MV) was adopted as a post-processing step to determine the final decision [21]. The class with the highest occurrence among the six results was predicted as the forthcoming locomotion mode.

In our proposed methods, each toe-off moment of the leading leg initiates the predictions for that step. Following this initial toe-off trigger, subsequent predictions can be made at specific times that conform to 20 ms intervals post toe-off. This paper only showcases prediction results with delays of 0 ms, 100 ms, 200 ms, 300 ms, and 400 ms from toe-off.

It should be noted that during the training process, all 850 ms of data were utilized to train the model, but during the prediction process, only the data within the selected prediction window were used for making a prediction.

TABLE I  
TRANSITIONS TO PREDICT

Transition Scenarios	Number	Transition Types
Transition From Level Walking (LW)	1	LW-LW
	2	LW-SA
	3	LW-SD
	4	LW-SS
Transition From Stair Ascent (SA)	5	SA-LW
	6	SA-SA
	7	SA-SS
Transition From Stair Descent (SD)	8	SD-LW
	9	SD-SD
	10	SD-SS
Transition From Standing Still (SS)	11	SS-LW
	12	SS-SA
	13	SS-SD

### C. Transition Definitions

**1) Transition Types:** In Section I, we stated that locomotion states can generally be divided into steady states and transitional states. However, our proposed method will not differentiate between them. We consistently focus on predicting the upcoming locomotion mode following the leading leg's toe-off moment, irrespective of whether it is identical to the preceding mode (steady state) or not (transitional state). This is because, in practice, it is impossible to know in advance whether the next step is in the same locomotion mode as the previous step or not. Therefore, for prediction purposes, each step could always be treated as a transition when predicting at the toe-off moment.

Based on this consideration, we further define the transition period as the interval from toe-off to the subsequent heel-strike, which corresponds to each swing phase of the instrumented leg, lasting approximately 500 ms in our experiments. This applies to each walking step, encompassing not only shifts between but also within the four steady state modes—level walking, stair ascent, stair descent, standing still. Predictions were made within each of these transition periods and consequently, a total of 13 types of transitions were examined, as detailed in Table I.

**2) Transition Scenarios:** A key feature of human ambulation is that the next locomotion mode is often constrained by the current mode. For instance, when in the stair ascent mode, the likely subsequent modes include stair ascent, level walking, or standing still, but rarely stair descent. Exploiting this feature by limiting the modes to predict could enhance prediction accuracy.

In this study, we assume the current locomotion mode is known, termed prior knowledge. Our objective is to determine the subsequent locomotion mode based on this prior knowledge. As a result, we grouped the 13 transition types into four transition scenarios (Table I): transitions from level walking (LW scenario), stair ascent (SA scenario), stair descent (SD scenario), and standing still (SS scenario). One approach to apply this to classification is training separate models for each scenario [22], but this is inefficient as the number of models increases with the number of scenarios to predict.

Instead, we trained a single model using data from all scenarios but made predictions based solely on the current scenario. For example, when the current scenario is LW, our

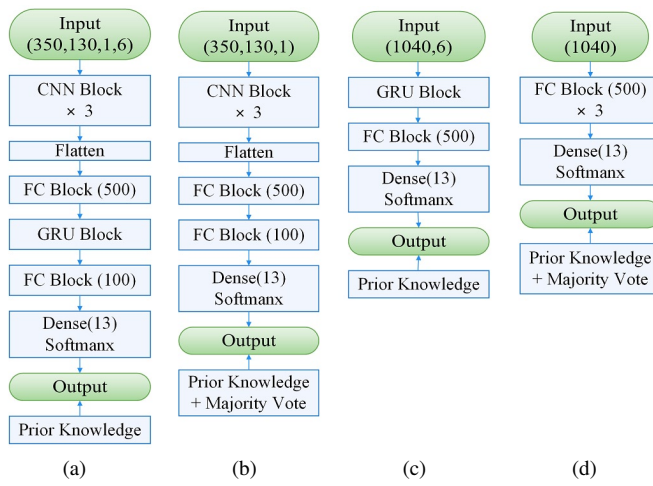


Fig. 3. Model structures. (a) CNN feature + GRU method (b) CNN feature + MV method (c) Manual feature + GRU method (d) Manual feature + MV method. Each CNN block contained a 2D convolutional layer (output channel=32, kernel size=3, stride=2, dilation=2), a batch normalization layer, a ReLU layer, and an average pooling layer (kernel size = 2). Each GRU block contained two GRU layers (hidden units = 1000). Each FC block contained a dense layer, a batch normalization layer, a ReLU layer, and a dropout layer (dropout rate = 0.5). The prior knowledge and majority vote method (when needed) were applied to the model output in order to get the final prediction results.

predictions only focus on four transitions LW-LW, LW-SA, LW-SD, and LW-SS (see Table I). While the model outputs probabilities for all 13 transition types, we limit our prediction to these four. Specifically, the transition type with the highest probability among these four is chosen as the prediction result, irrespective of the probabilities of other types in the SA, SD, and SS scenarios. Preliminary results showed that this method has comparable performance to the previous method.

#### D. Model Structures

By combining the two feature extraction methods and two prediction decision methods introduced in III-B, four distinct models were employed for prediction: CNN feature + GRU method, CNN feature + MV method, Manual Feature + GRU method, and Manual Feature + MV method. The structures of all models are shown in Fig. 3.

A five-fold cross-validation method was employed to train and test the models for each subject individually, with the training set shuffled and the test set unshuffled. Input data were standardized to achieve zero mean and unit variance before being fed into the classification models. Input data shapes and hyperparameters varied across models, with important hyperparameters (fine-tuned for each model) in Table II.

1) *CNN Feature and GRU Method*: The input data had a shape of [350, 130, 1, 6], where 350 denotes the 350 ms feature window size, and 130 represents the data from 130 channels across two muscles. The  $350 \times 130 \times 1$  forms a temporal-spatial EMG image with the image depth of one for the CNN model input. The number 6 corresponds to the six consecutive feature windows, and the feature vectors extracted from them served as a sequence input for the GRU layer. The model's output was a Softmax vector comprising 13 probabilities,

TABLE II  
HYPERPARAMETERS FOR EACH MODEL

Hyperparameters	CNN-GRU	CNN-MV	Manual-GRU	Manual-MV
number of epochs	15	50	50	100
mini-batch size	224	1024	1024	1024
lr decay rate	0.1	0.1	0.3	0.3
lr drops every N epochs	10	20	30	30

For all models, the Adam optimizer and the cross entropy loss function were utilized, the regularization parameter was set to 0.0001 and the initial learning rate (lr) was 0.01. The models were trained by Pytorch (v. 1.12.1).

each corresponding to a transition type. Subsequently, the final prediction was derived in conjunction with the prior knowledge method.

2) *CNN Feature and MV Method*: The input data had a shape of [350, 130, 1], with parameters of the same meaning as the first method. The only difference is that input feature windows were not combined sequentially, resulting in each extracted feature vector being independent of others. For each input, the model generated a Softmax vector comprising 13 probabilities, with the prediction result derived using the prior knowledge method. Then, the results from six consecutive inputs were aggregated via majority voting to yield the final prediction.

3) *Manual Feature and GRU Method*: The input data had a shape of [1040, 6]. For each electrode channel, eight manual features were extracted, resulting in 1040 features from 130 electrode channels as a feature vector. The six feature windows produced a sequence of six feature vectors as the input for the GRU layer. The processing of the model output in this method is the same as the CNN Feature + GRU Method.

4) *Manual Feature and MV Method*: The input data had a shape of 1040, with the parameter of the same meaning as the last method. Each feature vector was input to the model independently. The processing of the model output in this method is the same as the CNN Feature + MV Method.

#### E. Channel Manipulation

Utilizing 65 channels per muscle demands substantial computational resources. To investigate if using fewer channels could maintain performance, the HDsEMG channel count was reduced (in both training and test sets) for evaluation. This evaluation aimed to provide insights into the optimal quantity and density of electrodes.

1) *Reducing Channel Numbers*: Two methods were employed to reduce channels per muscle: maintaining density while reducing muscle coverage, and retaining muscle area with decreased density, as shown in Fig. 4. Particularly, for the two-electrode case, bipolar EMG signals were obtained by calculating the monopolar voltage difference between the two electrodes.

To assess performance with fewer channels, both the training set and test set employed identical channel configurations. Importantly, when the CNN feature-based methods were utilized for prediction, the employment of CNN blocks was constrained by input data size, necessitating adaptation as the number of channels decreased, as outlined in Table III.

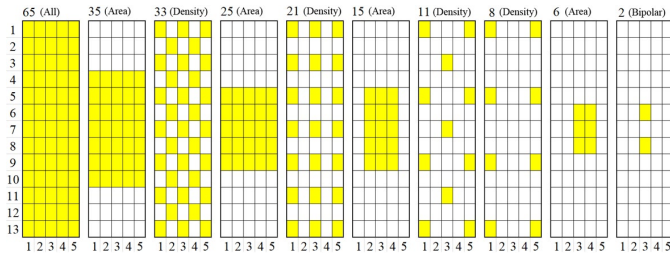


Fig. 4. Electrode reduction by area or density (as denoted on the top of each image). The numbers above the images signify the retained electrode count. Each square symbolizes a monopolar electrode on the grid, and yellow blocks represent retained electrodes. Both muscles share the same electrode configurations.

TABLE III  
ADJUSTED MODELS FOR REDUCED CHANNEL NUMBER

Channels	(50, 130]	(20, 50]	(2, 20]	[1,2]
CNN	2D CNN	2D CNN	2D CNN	1D CNN
Blocks	Block $\times$ 3	Block $\times$ 2	Block $\times$ 1	Block $\times$ 3

Channels are the total channel count on both muscles. Only the CNN blocks were modified, with other layers unchanged. Specifically, for the bipolar EMG, input data size of [350, 2, 1] rendered 2D CNN blocks inapplicable, and we use 1D CNN blocks instead. Each 1D CNN block comprised a 1D CNN layer (output channel=32, kernel size=3, stride=2, dilation=2), a batch norm layer, a ReLU layer, and an average pooling layer (kernel size = 2).

**2) Reducing Muscle Groups:** The total channel count also depends on the number of muscles measured. To evaluate the performance of using different muscle groups, prediction results were obtained from 65-channel HDsEMG on both the RF and TA muscles, as well as individually for either the RF or TA muscle.

In addition, results from bipolar EMG were also obtained for the same muscle groups. HDsEMG is expected to exhibit superior performance due to its yielding more comprehensive information than conventional bipolar EMG. The extent of prediction enhancement offered by HDsEMG over bipolar EMG is of interest.

#### F. HDsEMG Channel Recovery

Bipolar EMG electrodes may detach from the muscle during walking, leading to the loss of the entire muscle's signals and significantly affecting the results. In contrast, HDsEMG grids rarely detach completely during walking, although some channels may be disconnected, which results in a recording of zero value for these lost channels. We may recover the missing signals from the remaining channels to some extent.

**1) Selected Channel Loss:** In this study, to evaluate performance changes when the HDsEMG signals are partially lost, various numbers of bad channels were artificially introduced in the test set while keeping the original training set unchanged. Specifically, we examined two typical scenarios of channel loss: random channel loss and corner channel loss. Random channel loss refers to the loss of dispersed channels occurring randomly across the grid, while corner channel loss involves the loss of all channels in a poorly attached grid corner (only one corner was examined in this paper as a representative). The channel loss schemes are illustrated in Fig. 5.

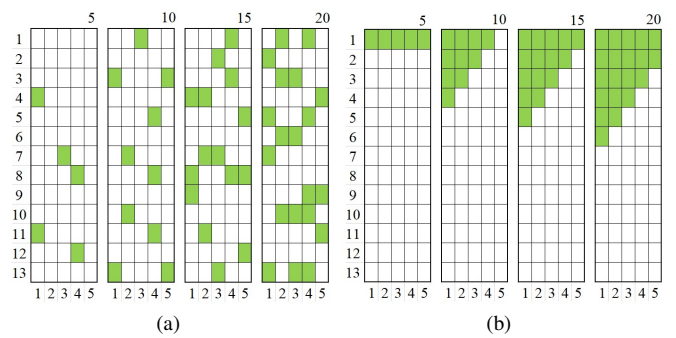


Fig. 5. Channel loss scheme illustration: (a) random loss, (b) corner loss. The numbers above the images indicate the lost electrode count. Each square represents a monopolar electrode on the HDsEMG grid, with green blocks indicating lost electrodes. A 20-channel loss constitutes 30% of the total channels, typically the maximum number encountered in practice. Both muscles share identical electrode configurations.

**2) Channel Recovery Method:** HDsEMG signals can be considered as images, enabling the application of image inpainting methods for recovering missing channel values.

Image inpainting methods can be classified into two categories: texture synthesis method and diffusion-based method [23]. The texture synthesis method learns the texture from similar regions or known image parts. In contrast, the diffusion-based method propagates from known local structures to the missing regions. Since muscle activity textures are typically non-repeating, this study employed the diffusion-based method, where partial differential equations (PDEs) are primarily used.

In this research, we utilized the biharmonic image inpainting method, a diffusion-based method, through the built-in Python scikit-image package (`skimage.restoration.inpaint_biharmonic`) to recover missing data. This method is based on the biharmonic equation, a fourth-order PDE, aiming to minimize the difference between the Laplacian of the inpainted image and the original image. For more technical details of the implemented image-inpainting method, please refer to [24], [25]. This method offers the advantages of being simple and fast to implement while producing smooth and visually coherent results. We used it to restore the missing channels in HDsEMG signals based on the remaining channels and evaluated the performance before and after recovery.

#### G. Performance Evaluation

The model prediction performance is quantified by prediction accuracy, the ratio of correctly classified test labels to the total number of test labels, which is commonly used in multi-class classification problems. Each subject's model was trained independently, with the overall accuracy averaged across subjects.

We examined the prediction accuracy among different methods and conditions, including different classification models, various time delays since toe-off, varying numbers of channel reductions, channel loss and recovery, using paired t-tests with Bonferroni correction to determine the statistical significance of performance differences. In subsequent plots, "\*" and "\*\*" will be utilized to denote statistically significant differences

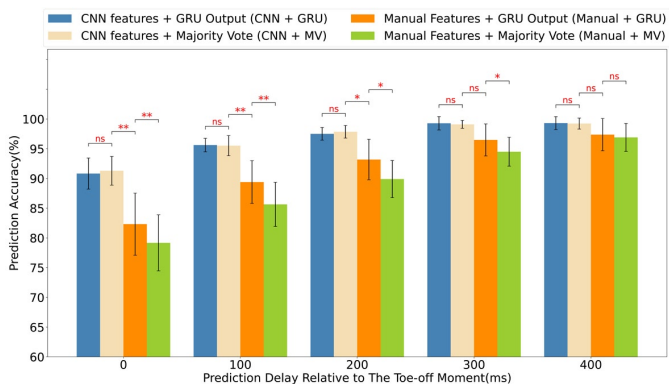


Fig. 6. Prediction accuracy of different classification methods with varied delays. The error bars represent standard deviations across subjects.

at the  $p < 0.05$  and  $p < 0.01$  levels, and "ns" means "not statistically significant".

## IV. RESULTS

### A. Model Performance

Fig. 6 presents the prediction accuracy of four distinct models as detailed in Section III-D: CNN + GRU method, CNN + MV method, Manual + GRU method, and Manual + MV method.

All models demonstrated improved accuracy as the delay increased. For example, The CNN + MV method achieved an accuracy of  $91.1\% \pm 2.4\%$  at toe-off, which rose to  $95.6\% \pm 1.1\%$  and  $98.9\% \pm 0.7\%$  when the delays increased to 100 ms and 300 ms respectively. A further minor improvement to  $99.2\% \pm 0.9\%$  was noted at the 400 ms delay, which is close to the foot strike moment. A similar trend was observed for other methods as well.

It was also observed that the two CNN-feature methods exhibited better prediction performance than the two Manual-feature methods. At toe-off, the CNN-feature methods demonstrated statistically significant higher accuracy ( $p < 0.01$ ), approximately 91%, compared to Manual-feature methods, which showed around 80% accuracy. This advantage lessened with increasing delay; at a 400 ms delay, their accuracies became close (99% vs. 97%).

Moreover, compared to Manual-feature models, the CNN-feature models demonstrated greater performance consistency, exhibiting only half the variance in accuracy among subjects. As delay increased, the accuracy variance tended to decrease for all models, indicating more stable prediction performance.

The GRU module's impact varied across different models. In Manual-feature methods, incorporating GRU resulted in a statistically significant improvement of approximately 4% in prediction accuracy at delays of 0 ms, 100 ms, and 200 ms. However, It did not show improved prediction accuracy when teamed with CNN-feature models.

To summarize, the CNN + MV method outperformed the two Manual-feature methods, and exhibited comparable performance to the CNN + GRU method while requiring less computational power. It will be utilized to generate the prediction results in subsequent sections.

### B. Transition Accuracy

Fig. 7 presents the confusion matrices derived from the CNN + MV method, illustrating the results at several specified prediction delay points. The confusion matrices detailed the accuracies for all transitions, which presented various degrees of predictability for different transitions (classified as four scenarios, see Table I).

When predicted at toe-off (0 ms delay), the model performed optimally in the SS scenario (all transitions above 92%) and also performed satisfactorily in the LW scenario (except for the LW-SD transition, with 86.4% accuracy). Conversely, the model in the SD scenario performed the worst, with the SD-SS transition presenting the lowest accuracy of 72.1%.

With a 100 ms delay, the model performance significantly improved in most scenarios (LW, SA, SS), achieving accuracies above 90% for all their transitions, except in the SD scenario. While SD also showed improvement, it remained the least accurate, with the SD-SS transition having the lowest accuracy at 77.7%. The most notable enhancement was in the SA scenario, where the SA-LW transition accuracy dramatically increased from 84.3% to 98.7%.

A significant improvement in the SD scenario occurred at the 200 ms delay, with the SD-SS transition accuracy rising to 89.6%, and the other two transitions exceeding 95%. By the 300 ms delay, all transitions could be classified with high accuracy, with even the lowest accuracy of 97.2% (for the SD-SS transition).

### C. Reduced Channels

Fig. 8 illustrates the prediction accuracy of different channel counts as determined by the channel reduction scheme presented in Fig. 4. For clarity, only 0 ms, 200 ms and 400 ms were displayed in the figure. As expected, accuracy improved with increasing delay, across all channel counts. Three aspects were identified when examining the effect of channel reduction on prediction accuracy.

Firstly, the prediction accuracy generally decreased as the channel count decreased, but the relationship was nonlinear. For example, at toe-off (0 ms delay), halving the channel number to 35 (from 65) resulted in only a minor accuracy drop (from  $91.1\% \pm 2.4\%$  to  $89.8\% \pm 3.5\%$ , without statistical significance). A substantial impact was observed only when the channel count was further reduced to 15, with accuracy falling to  $85.6\% \pm 4.5\%$  ( $p < 0.01$ ).

Secondly, the influence of channel count reduction on accuracy lessened with increased prediction delay. For instance, the accuracy of using 15 channels declined by only 1% at a 400 ms delay, with the difference being statistically insignificant.

Lastly, the two methods of reducing channel number (by area or by density) did not show a significant difference in model performance, but subtle differences were discernible upon closer examination. For instance, when examining the toe-off moment, 11 channels reduced by density were instead 1% more accurate than 15 channels reduced by area, although this was not significant.

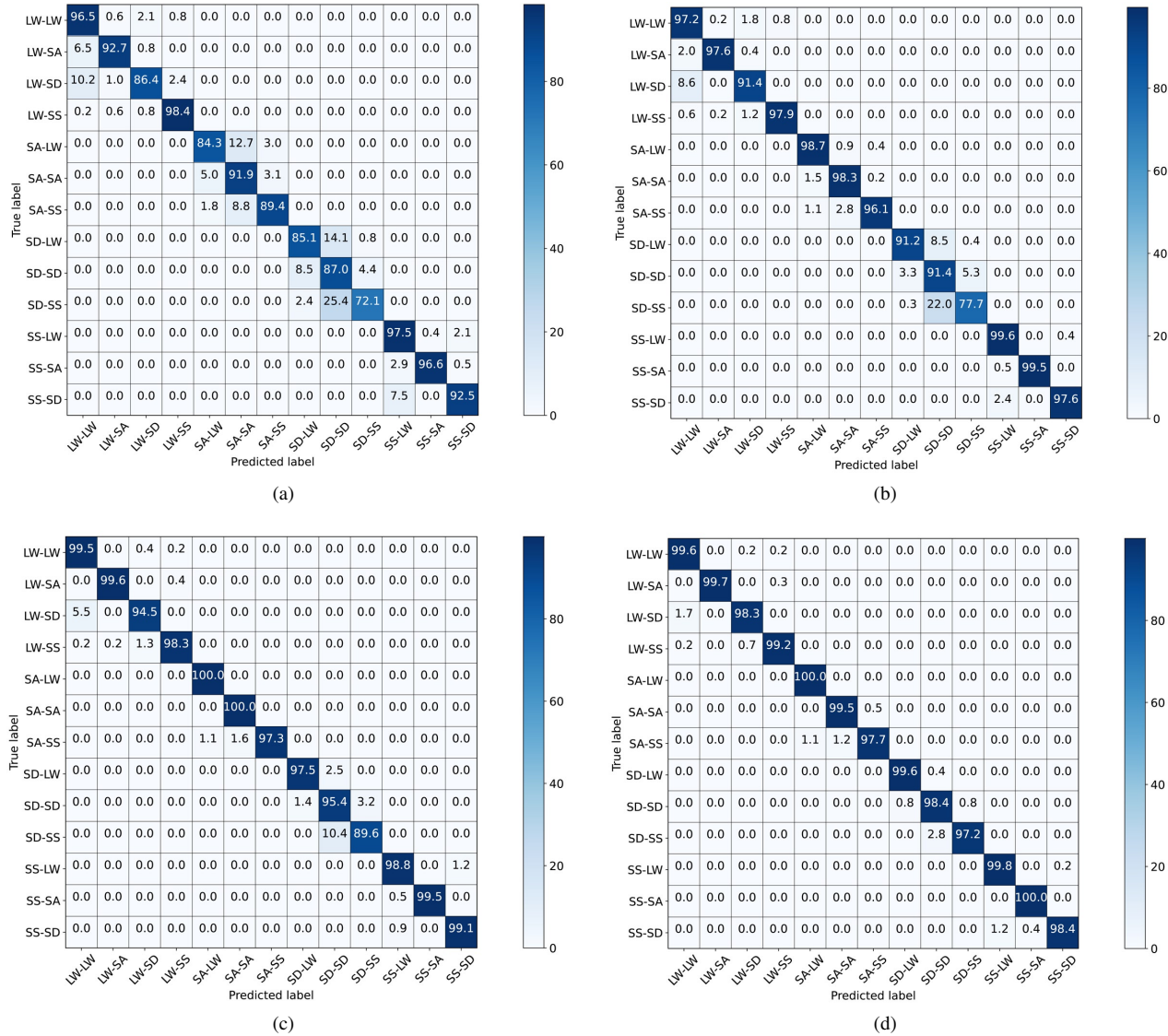


Fig. 7. Confusion matrix at selected prediction delay points relative to the toe-off moment. (a) 0 ms, (b) 100 ms, (c) 200 ms, (d) 300 ms. The 400 ms delay is not displayed as it has similar results as the 300 ms delay.

#### D. Muscle groups

Fig. 9 shows the impact of HDsEMG and bipolar EMG measurements across various muscle groups on the prediction accuracy. Using HDsEMG on both muscles yielded statistically significant ( $p < 0.05$ ) higher accuracy than on a single muscle (e.g., 5% enhancement observed when predicting at toe-off). This advantage diminished with increasing delay, becoming statistically not significant at 400 ms. Additionally, using HDsEMG on the TA muscle performed better than on the RF muscle, although the superior performance was marginal, approximately 1%-2% across all delays.

Furthermore, HDsEMG consistently outperformed bipolar methods across all muscle groups and delays. Particularly, when predicting at toe-off, a substantial improvement of approximately 20% was observed in all muscle groups. Although this improvement narrowed with increasing delays, there still remained a considerable gap of 10% at the 400 ms delay. Additionally, HDsEMG exhibited considerably lower variance

in prediction accuracy compared to bipolar EMG (e.g., approximately half the variance across subjects at toe-off), indicating a more stable performance.

#### E. Channel Recovery

Fig. 10 presents the prediction results for channel loss and recovery, derived from the two channel-loss schemes illustrated in Fig. 5. Note that the model here was trained on the original full-channel dataset but tested on the dataset with lost channels, which differs from IV-C, where the model was both trained and tested using a reduced-channel dataset.

It was found that the channel loss issue resulted in significant accuracy drops. For instance, the loss of just five channels led to a drastic 20% decrease in accuracy, from over 90% to around 70%, in both random and corner loss scenarios at toe-off. Furthermore, with an increased number of lost channels, the performance drop exceeded 40% in the worst cases (20 lost channels in both scenarios). Although this decrease diminished

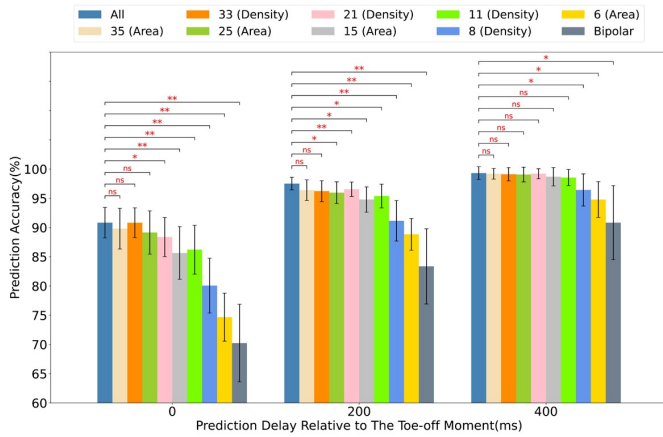


Fig. 8. Effect of channel number and delay on prediction accuracy. In the legend, "Numbers" means the retained channels per muscle; (Area) and (Density) denotes reducing channels by muscle area or electrode density. The error bars represent standard deviations across subjects.

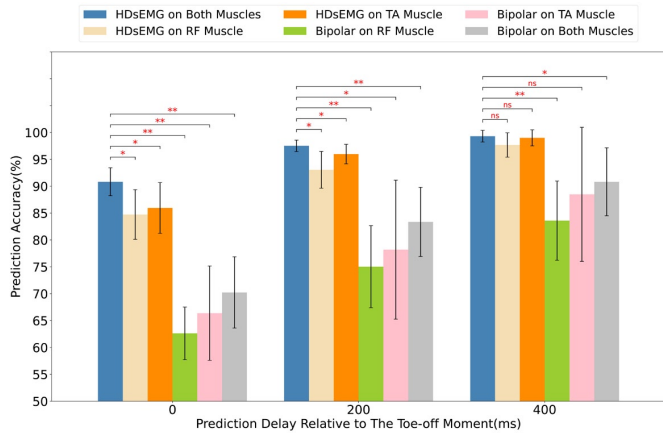


Fig. 9. Prediction accuracy of HDsEMG and bipolar EMG across different muscle groups and delays. The error bars represent standard deviations across subjects.

with delay, there was still a notable 20% drop in accuracy at a 400 ms delay.

By implementing the image inpainting method to recover missing data, the accuracy drop could be considerably compensated. In the random loss scenario, no statistically significant decrease in accuracy was observed after recovery across all conditions (including all number of lost channels and delays). In contrast, the corner loss scenario exhibited marginally inferior performance. Although accuracy could be restored in most situations, a statistically significant decline ( $p < 0.01$ ) could be observed when 20 channels were lost, at the early prediction stages (0 ms, 100 ms delay). Nonetheless, this decrease was still minimal, a mere 3% accuracy drop after recovery compared to a substantial 45% drop without recovery.

## V. DISCUSSION

### A. Model Comparison

The comparative analysis in Section IV-A (refer to Fig. 6) revealed that CNN-feature methods outperform manual-feature methods. Although conventional manual features showed effectiveness for predictions at later delay points, such as near

heel-strike, their predictive ability at the early stages of transitions was limited. In contrast, CNN models, leveraging both spatial and temporal information from HDsEMG signals, significantly enhanced prediction accuracy, particularly at initial transition stages. This underscores the advantages of using CNN-based methods for training the prediction models.

We argue that CNN-derived features are superior to those obtained through manual methods. To further investigate this matter, we utilized principal component analysis (PCA) for visualization and comparison. Since CNN model-derived features are images, incompatible with manual feature vectors, we flattened the CNN-extracted features for comparison. After extracting and flattening the activation outputs from the final CNN block, we applied PCA to both CNN-based and manual feature vectors for dimensionality reduction. The first three components were selected and depicted in Fig. 11.

The components from CNN features (Fig. 11a) exhibited greater separability compared to the entangled components from manual features (Fig. 11b). This comparison supports the superiority of CNN-extracted features and provides an intuitive evidence for the CNN method's enhanced performance over the manual method.

The GRU module was anticipated to enhance prediction accuracy by capturing additional temporal information. However, according to the results in Fig. 6, it proved true for manual-feature methods but not for CNN-feature methods. This is likely because our CNN models already efficiently incorporated temporal information, leaving limited room for the GRU module to offer further improvement.

### B. Transition Analysis

According to the analysis in Section IV-B, the four transition scenarios in Table I can be ranked in the order of predictability as follows: SS scenario, LW scenario, SA scenario, and SD scenario. Note that we primarily focused on the overall accuracy change pattern at varying delays. Generally, we observed that accuracy increased with longer delays for each specific transition type. However, some exceptions could be found in Fig. 7, such as LW-SS (100ms to 200ms) decreasing by 0.5%, SA-SA (200ms to 300ms) by 0.5%, SS-LW (100ms to 200ms) by 0.8%, and SS-SD (200ms to 300ms) by 0.7%. These declines were minimal (less than 1%) and the accuracies fluctuated around a high level (99%). We argue that they were likely attributable to data randomness due to the variability of EMG signals.

The SS scenario was the most predictable, involving transitions from static to dynamic activities. Since the body is in a stationary state during standing still, there are distinct changes in body posture and muscle activation patterns when the body starts to move. Thus, muscle signal changes preceding the movement can be relatively easily identified, resulting in high early-stage prediction accuracy around toe-off.

The LW scenario was the second easiest to predict. During level walking, the body exhibits a relatively stable and rhythmic pattern of dynamic movement, with a consistent gait cycle. Transitions from level walking to other activities involve noticeable changes in the gait pattern and muscle

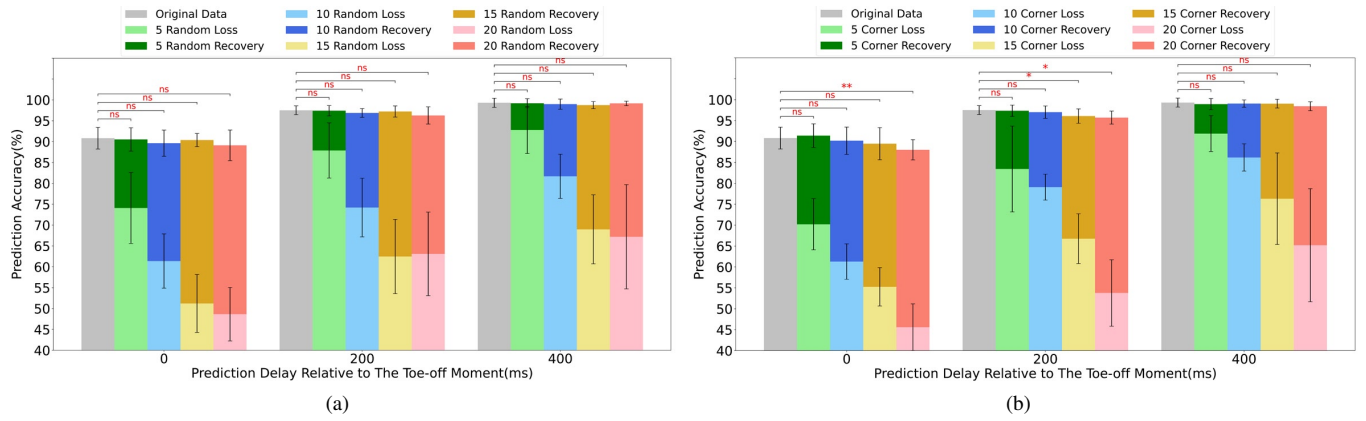


Fig. 10. Effect of channel loss and recovery on prediction accuracy across different delays. (a) random channel loss accuracy before and after recovery (b) corner channel loss accuracy before and after recovery. The bottom segment of the bar represents the baseline accuracy before recovery, while the upper segment of the bar showcases the additional accuracy compensated by recovery. The error bars represent standard deviations across subjects. Note: significance annotations denote the statistical relevance of post-recovery values only.

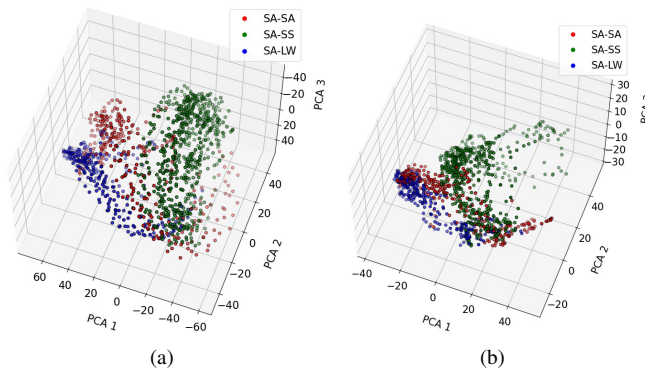


Fig. 11. The first three PCA components of features. (a) CNN-extracted features, (b) manually extracted features. The representative data samples are from the test set of one subject performing the SA scenario transitions, including SA-SA, SA-SS, and SA-LW.

activation, facilitating early prediction. However, the LW-SD transition within the LW scenario poses a challenge, likely because the initial period following the toe-off moment of the LW-SD transition still resembles level walking conditions. This similarity often results in misclassification as the LW-LW transition. As the transition progresses, the walking pattern gradually shifts toward stair descent and leads to higher accuracy.

In the SA scenario, the prediction accuracy started off low but improved significantly after a delay of 100ms. This may be attributed to the necessity of an initial foot lift to clear the step for transitions from stair ascent, irrespective of the subsequent mode (SA, LW, SS), causing initial difficulty in distinguishing transitions. However, after approximately 100 ms, the movement aligns closer with the next mode, yielding more discernible muscle activation patterns and higher prediction accuracy.

The SD scenario presented the greatest difficulty in transition prediction, especially for the SD-LW and SD-SS transitions, which were often misclassified as the SD-SD transition. This may stem from the leading leg (swing leg) not being the primary determinant of transitions during SD locomotion,

with the supporting leg playing a critical role and displaying substantial muscle signal changes. The supporting leg must flex in order to descend stairs [26], whereas the leading leg relies more on gravitational force, necessitating smaller voluntary muscle effort. This is distinct from the SA and LW scenarios, which usually require more muscle activation on the leading leg to lift the foot up for subsequent transitions. Consequently, the subtle muscle signal changes in the leading leg during SD locomotion make them difficult to distinguish at early transition stages. These findings also suggest that transition prediction performance may be further improved by measuring both legs.

### C. Effect of Channel Numbers

Fig. 8 demonstrates that increasing channel number helps improve the performance, especially for early stage prediction, as detailed in Section IV-C. However, increasing channels also incurs substantial computational costs, necessitating a trade-off between channel quantity and performance.

Our findings indicate that increasing the number of channels does not always improve performance. Generally, 21 channels are sufficient to achieve comparable results to 65 channels while consuming only around 30% of the computational power. Employing more channels offers marginal benefits but with a more substantial computational load.

The spatial distribution of increased channels is not very crucial, as accuracy generally improves when channel count increases regardless of the distribution. On the other hand, further observation indicates that sparse electrodes covering broader muscle areas slightly surpass dense electrodes on smaller areas, suggesting that measuring a broader range of muscle signals leads to relatively better prediction ability.

When early prediction is not critical, the required number of channel or muscle measurements can be further reduced. For example, when a 400 ms delay is acceptable, the channel count per muscle can be lowered to 10, with only a small compromise in performance compared to using 65 channels. Also, the number of muscles required for measurement can be reduced to only one.

Furthermore, the analysis of Fig. 9 in Section IV-D reveals that integrating more muscles could significantly enhance prediction performance, which is especially useful for improving early transition prediction ability. In our study, only two anterior leg muscles on a single leg were measured. It is anticipated that adding posterior leg muscles to form agonist-antagonist pairs, or incorporating recordings from both legs could further improve performance.

#### D. Robustness to Channel loss

Fig. 12 displays a single frame of original HDsEMG images alongside corresponding channel loss and post-recovery images. Panels (a) and (b) respectively show corner channel loss post- and pre-recovery, while panels (d) and (e) depict random channel loss pre- and post-recovery. Overall, both post-recovery images in panels (a) and (e) closely resembled the original image shown in panel (c).

A closer examination revealed that data recovery in the corner loss scenario (see Fig. 12a) is less effective compared to the random loss scenario (refer to Fig. 12e). In the corner loss scenario, the lack of information around the [1,1] area led to an unsuccessful recovery of the signal there, yet the overall performance remained acceptable.

These observations were consistent with the results in Figure 10, where the recovery method effectively offset the accuracy reduction observed with 30% channel loss. This method demonstrated superior performance in the random loss scenario but also produced satisfactory outcomes in the corner loss scenario.

The results highlight an important benefit of HDsEMG over bipolar EMG: HDsEMG can recover missing signals based on the remaining channels, thereby significantly enhancing its robustness against the issue of lost channels; Conversely, bipolar EMG lacks the ability to regenerate lost signals, leading to complete signal loss of the muscle upon electrode detachment, and thus increasing the risk of misclassification and controller malfunction.

#### E. Comparison with Bipolar EMG

In this study, we hypothesized that employing HDsEMG could enhance locomotion prediction capability, especially during early transition stages. This is supported by the prediction results shown in Fig. 9, where HDsEMG achieved a significant increase in accuracy compared to bipolar EMG for the same muscle groups. The improved performance could be attributed to the following factors:

Firstly, HDsEMG measures more comprehensive muscle activation signals than bipolar EMG, as exemplified in Fig. 13. In panels (a) and (b), measurements on the TA muscle during different transitions yielded identical bipolar EMG values of 0.0076, yet the corresponding HDsEMG signal images exhibited considerably different patterns. The observations in panels (c) and (d) for the RF muscle indicated a similar discrepancy. Enhanced information provided by HDsEMG lays the foundation for distinguishing muscle activation patterns that bipolar EMG cannot detect, especially at early transition

stages, supporting the superior performance of HDsEMG in early transition prediction than bipolar EMG.

Secondly, HDsEMG enables the use of more advanced techniques, such as CNN methods and image recovery methods, to extract and restore valuable features from recorded signals. As discussed in Section V-A and Section V-D, the CNN method enables the extraction of both temporal and spatial features from HDsEMG, significantly enhancing prediction accuracy; the image recovery method leverages HDsEMG's rich spatial information, successfully restoring lost information to mitigate the decrease in accuracy.

Thirdly, models trained with HDsEMG exhibit more stable prediction performance. According to Fig. 9, bipolar EMG results have significantly higher variance than HDsEMG results. This is likely because bipolar EMG performance is significantly affected by electrode positions. Careful electrode placement is essential to obtaining high-quality EMG signals for each subject. However, identifying optimal locations is challenging, as it is sensitive to various subject-specific physiological factors. Suboptimal placement across subjects increases prediction variance and reduces overall accuracy. Conversely, HDsEMG, covering a larger muscle area, is more likely to encompass regions with high-quality signals, rendering it less position-sensitive and thus exhibiting increased stability across subjects for higher overall accuracy.

To summarize, bipolar EMG's inferior transition prediction performance may result from inadequate muscle signal measurement, inefficient feature extraction techniques, and improper electrode placement. These limitations could be mitigated by HDsEMG, enabling the trained models to effectively discern nuanced muscle signal changes, particularly during early transition stages, thereby substantially enhancing prediction capabilities.

## VI. CONCLUSION

In this study, we employed two HDsEMG sensors on the RF and TA muscles to investigate their effectiveness in detecting muscle activation changes for enhanced locomotion transition prediction. The results showed that compared to bipolar EMG on the same muscle, HDsEMG methods significantly improved transition prediction accuracy by around 20% at toe-off, showcasing HDsEMG's superior capability in detecting subtle activation changes during early transition stages. Additionally, through image-inpainting methods, HDsEMG demonstrated robustness to electrode loss, a common issue in dynamic walking, with only a 3% decrease in accuracy despite 30% electrode detachment.

Although this research employed two  $13 \times 5$  electrode grids to cover two muscles, the results showed that reducing electrode count to 21 per muscle only slightly reduced accuracy by around 3% at toe-off. We suggest that using just over 20 electrodes per muscle would be sufficient for balancing prediction performance and computational load, with relatively sparse electrode coverage of broader muscle areas preferred. Future studies could expand the measurements to encompass up to six muscles, using the same total number of electrodes as in this research, which could potentially yield greater accuracy without incurring extra computational demands.

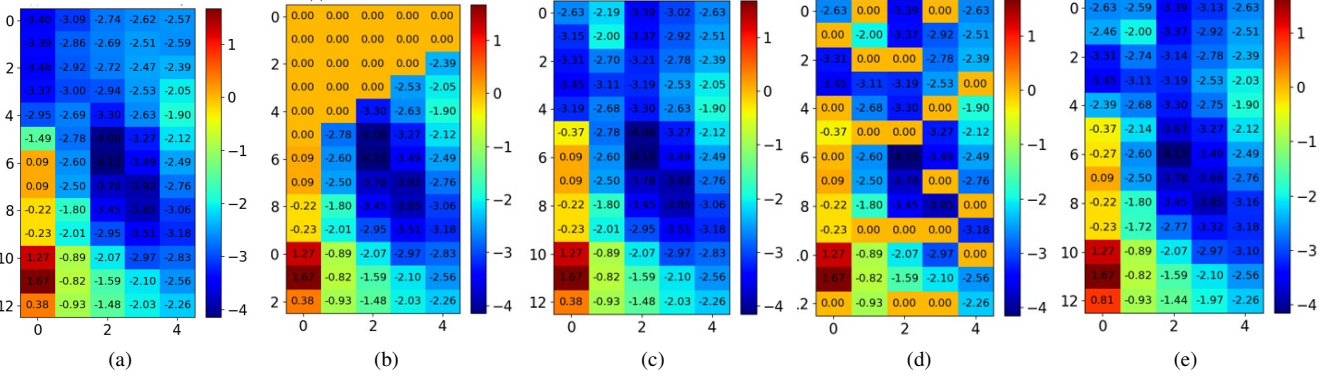


Fig. 12. HDsEMG signal examples with 20-channel loss and recovery: (a) corner loss recovery, (b) corner loss scenario (c) Original Signal (d) random loss scenario (e) random loss recovery. The electrode values near position [1,1] in the image array demonstrated superior recovery in the random scenario compared to the corner scenario. Data were standardized for model input.

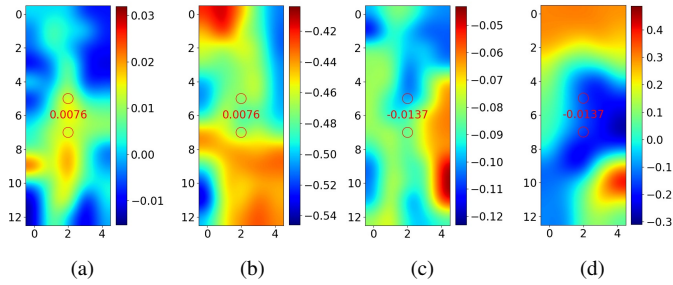


Fig. 13. Frames of HDsEMG and bipolar EMG around toe-off: (a) TA muscle during LW-LW transition, (b) TA muscle during LW-SA transition, (c) RF muscle during LW-LW transition, and (d) RF muscle during LW-SA transition. HDsEMG images were spatially interpolated using bicubic interpolation. Two red circles on each image represent two selected electrodes and the red number displays the bipolar EMG value derived from the two electrodes. Data were standardized for model input.

One limitation of this paper is that it only experimented with healthy individuals. Our future research will address clinical populations to further demonstrate the advantages of HDsEMG. Another limitation of this paper is that we conducted only offline data analysis. Our future research will extend the application to real-time processing, focusing on performance indicators such as prediction accuracy, processing time, power consumption, etc.

It is notable that in our proposed prediction method, we assumed the current locomotion mode was known, enabling a restriction of potential transitions to enhance accuracy. In practice, the current mode can be inferred from the prediction results of the preceding transition. However, early predictions may result in relatively low accuracy, which renders the identified current locomotion mode less reliable.

To improve the reliability of the current mode recognition, an additional prediction can be made at the end of the preceding transition, such as near the foot-strike. As demonstrated in our results (see Fig. 6), late prediction accuracy, for instance, 400 ms after toe-off, can be exceedingly high, exceeding 99%. This high accuracy provides a more reliable reference for confirming the current locomotion mode. This approach offers the potential for future studies to realize continuous and

accurate identification of locomotion intent during ambulation.

To conclude, this research demonstrated the superiority of HDsEMG in accurately detecting early locomotion transitions and enhancing robustness due to its substantial spatial information. The findings highlight its potential as a reliable source for accurate and robust locomotion prediction in future applications.

## ACKNOWLEDGMENT

The authors would like to thank all the subjects for their participation in the experiments.

## REFERENCES

- [1] H. Huang, F. Zhang, L. J. Hargrove, Z. Dou, D. R. Rogers, and K. B. Englehart, "Continuous locomotion-mode identification for prosthetic legs based on neuromuscular-mechanical fusion," *IEEE Transactions on Biomedical Engineering*, vol. 58, no. 10, pp. 2867–2875, Oct. 2011.
- [2] D. Xiong, D. Zhang, X. Zhao, Y. Chu, and Y. Zhao, "Learning non-euclidean representations with spd manifold for myoelectric pattern recognition," *IEEE Transactions on Neural Systems and Rehabilitation Engineering*, vol. 30, pp. 1514–1524, 2022.
- [3] J. Huang, S. Lin, N. Wang, G. Dai, Y. Xie, and J. Zhou, "Tse-cnn: A two-stage end-to-end cnn for human activity recognition," *IEEE Journal of Biomedical and Health Informatics*, vol. 24, no. 1, pp. 292–299, Jan. 2020.
- [4] F. Hu, H. Wang, N. Feng, B. Zhou, C. Wei, Y. Lu, Y. Qi, X. Jia, H. Tang, and M. A. Gouda, "A novel fusion strategy for locomotion activity recognition based on multimodal signals," *Biomedical Signal Processing and Control*, vol. 67, p. 102524, May 2021.
- [5] D. Xiong, D. Zhang, X. Zhao, Y. Chu, and Y. Zhao, "Synergy-based neural interface for human gait tracking with deep learning," *IEEE Transactions on Neural Systems and Rehabilitation Engineering*, vol. 29, pp. 2271–2280, 2021.
- [6] B.-Y. Su, J. Wang, S.-Q. Liu, M. Sheng, J. Jiang, and K. Xiang, "A cnn-based method for intent recognition using inertial measurement units and intelligent lower limb prosthesis," *IEEE Transactions on Neural Systems and Rehabilitation Engineering*, vol. 27, no. 5, pp. 1032–1042, May 2019.
- [7] J. Camargo, W. Flanagan, N. Csomay-Shanklin, B. Kanwar, and A. Young, "A machine learning strategy for locomotion classification and parameter estimation using fusion of wearable sensors," *IEEE Transactions on Biomedical Engineering*, vol. 68, no. 5, pp. 1569–1578, May 2021.
- [8] Y.-X. Liu, R. Wang, and E. M. Gutierrez-Farewik, "A muscle synergy-inspired method of detecting human movement intentions based on wearable sensor fusion," *IEEE Transactions on Neural Systems and Rehabilitation Engineering*, vol. 29, pp. 1089–1098, 2021.

- [9] B. Hu, E. Rouse, and L. Hargrove, "Fusion of bilateral lower-limb neuromechanical signals improves prediction of locomotor activities," *Frontiers in Robotics and AI*, vol. 5, p. 78, 2018.
- [10] J. A. Spanias, A. M. Simon, S. B. Finucane, E. J. Perreault, and L. J. Hargrove, "Online adaptive neural control of a robotic lower limb prosthesis," *Journal of Neural Engineering*, vol. 15, no. 1, p. 016015, Jan. 2018.
- [11] R. Merletti and S. Muceli, "Tutorial. surface emg detection in space and time: Best practices," *Journal of Electromyography and Kinesiology*, vol. 49, p. 102363, Dec. 2019.
- [12] W. Geng, Y. Du, W. Jin, W. Wei, Y. Hu, and J. Li, "Gesture recognition by instantaneous surface emg images," *Scientific Reports*, vol. 6, no. 1, p. 36571, Nov. 2016.
- [13] X. Chen, Y. Li, R. Hu, X. Zhang, and X. Chen, "Hand gesture recognition based on surface electromyography using convolutional neural network with transfer learning method," *IEEE Journal of Biomedical and Health Informatics*, vol. 25, no. 4, pp. 1292–1304, Apr. 2021.
- [14] S. Jing, H.-Y. Huang, R. Vaidyanathan, and D. Farina, "Accurate and robust locomotion mode recognition using high-density emg recordings from a single muscle group," in *2022 44th Annual International Conference of the IEEE Engineering in Medicine & Biology Society (EMBC)*, Jul. 2022, pp. 686–689.
- [15] H. J. Hermens, B. Freriks, R. Merletti, D. Stegeman, J. Blok, G. Rau, C. Disselhorst-Klug, and G. Hägg, "European recommendations for surface electromyography," *Roessingh research and development*, vol. 8, no. 2, pp. 13–54, 1999.
- [16] A. Pachi and T. Ji, "Frequency and velocity of people walking," *Struct. Eng.*, vol. 83, no. 3, pp. 36–40, 2005.
- [17] P. Tsinganos, B. Cornelis, J. Cornelis, B. Jansen, and A. Skodras, "Data augmentation of surface electromyography for hand gesture recognition," *Sensors*, vol. 20, no. 17, p. 4892, Aug. 2020.
- [18] B. Hudgins, P. Parker, and R. Scott, "A new strategy for multifunction myoelectric control," *IEEE Transactions on Biomedical Engineering*, vol. 40, no. 1, pp. 82–94, Jan. 1993.
- [19] J. A. Spanias, A. M. Simon, S. B. Finucane, E. J. Perreault, and L. J. Hargrove, "Online adaptive neural control of a robotic lower limb prosthesis," *Journal of Neural Engineering*, vol. 15, no. 1, p. 016015, Jan. 2018.
- [20] A. Phinyomark, P. Phukpattaranont, and C. Limsakul, "Feature reduction and selection for emg signal classification," *Expert Systems with Applications*, vol. 39, no. 8, pp. 7420–7431, Jun. 2012.
- [21] K. Englehart and B. Hudgins, "A robust, real-time control scheme for multifunction myoelectric control," *IEEE Transactions on Biomedical Engineering*, vol. 50, no. 7, pp. 848–854, Jul. 2003.
- [22] A. J. Young and L. J. Hargrove, "A classification method for user-independent intent recognition for transfemoral amputees using powered lower limb prostheses," *IEEE Transactions on Neural Systems and Rehabilitation Engineering*, vol. 24, no. 2, pp. 217–225, Feb. 2016.
- [23] C. Guillemot and O. Le Meur, "Image inpainting : Overview and recent advances," *IEEE Signal Processing Magazine*, vol. 31, no. 1, pp. 127–144, Jan. 2014.
- [24] S. B. Damelin and N. S. Hoang, "On surface completion and image inpainting by biharmonic functions: Numerical aspects," *International Journal of Mathematics and Mathematical Sciences*, vol. 2018, pp. 1–8, 2018.
- [25] C. K. Chui and H. Mhaskar, "Mra contextual-recovery extension of smooth functions on manifolds," *Applied and Computational Harmonic Analysis*, vol. 28, no. 1, pp. 104–113, 2010.
- [26] M. Grimmer, J. Zeiss, F. Weigand, G. Zhao, S. Lamm, M. Steil, and A. Heller, "Lower limb joint biomechanics-based identification of gait transitions in between level walking and stair ambulation," *PLOS ONE*, vol. 15, no. 9, p. e0239148, Sep. 2020.